ACS APPLIED MATERIALS & INTERFACES

Research Article

www.acsami.org

Anhydrous Phosphoric Acid Functionalized Sintered Mesoporous Silica Nanocomposite Proton Exchange Membranes for Fuel Cells

Jie Zeng,[†] Beibei He,[†] Krystina Lamb,[‡] Roland De Marco,[‡] Pei Kang Shen,[§] and San Ping Jiang*,[†]

[†]Fuels and Energy Technology Institute & Department of Chemical Engineering, Curtin University, Perth, WA 6102, Australia

[‡]Faculty of Science, Health, Education and Engineering, University of the Sunshine Coast, Maroochydore DC, Queensland 4558, Australia

[§]Advanced Energy Materials Laboratory, Sun Yet-sen University, Guangzhou 510275, China

ABSTRACT: A novel inorganic proton exchange membrane based on phosphoric acid (PA)-functionalized sintered mesoporous silica, PA-*meso*-silica, has been developed and investigated. After sintering at 650 °C, the *meso*-silica powder forms a dense membrane with a robust and ordered mesoporous structure, which is critical for retention of PA and water within the porous material. The PA-*meso*-silica membrane achieved a high proton conductivity of 5×10^{-3} to 5×10^{-2} S cm^{-1} in a temperature range of 80−220 °C, which is between 1 and 2 orders of magnitudes higher than a typical membrane Nafion 117 or polybenzimidazole (PBI)/PA in the absence of external humidification. Furthermore, the PA-*meso*-silica membranes exhibited good chemical stability along with high performance at elevated temperatures, producing a peak power density of 632 mW cm^{-2} using a H_2 fuel at 190 °C in the absence of external humidification. The high membrane proton conductivity and excellent fuel cell performance demonstrate the utility of PA-*meso*-silica as a new class of inorganic proton exchange membranes for use in the high-temperature proton exchange membrane fuel cells (PEMFCs).

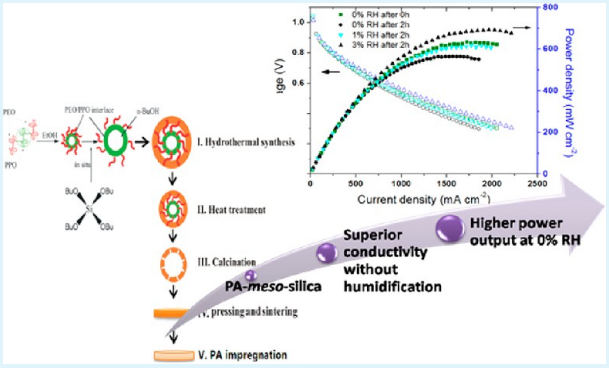

KEYWORDS: *sintered mesoporous silica, phosphoric acid, high-temperature proton exchange membrane, fuel cells*

1. INTRODUCTION

Today, electricity is the most convenient form of energy. For the past 100 years, electricity has been primarily produced by the combustion of fossil fuels, which has an intrinsically low conversion efficiency and emits greenhouse gases, such as carbon dioxide, and other air pollutants. With increasing energy demand, depleting fossil fuel reserves, and growing concerns about air pollution and the environment, there is an urgent need to increase electricity generation efficiency and to develop renewable energy sources. Fuel cells are energy conversion devices capable of converting electrochemically the chemical energy of fuels, such as hydrogen, methanol, ethanol, natural gas, and hydrocarbons, into electricity, so fuel cells inherently have a significantly higher efficiency compared to conventional energy conversion technologies, such as internal combustion engines. Among various types of fuel cells, proton exchange membrane fuel cells (PEMFCs) are the most promising energy sources for portable applications due to their high energy density, ease of transportation, and storage of liquid fuels.[1−3] PEM fuel cells demand membrane materials that must be chemically stable, provide structural support, and have low permeability to diffusing reactants and product species, as well as possessing high proton conductivity. Currently, state-of-the-art PEMs, such as Nafion with interconnected hydrophilic domains, have excellent chemical, mechanical, and thermal stability and high proton conductivity when fully hydrated,[4,5] but are quite permeable to water and methanol.[6,7] The methanol crossover from the anode to cathode through the Nafion membrane reduces the open-circuit potential by as much as 0.15−0.2 V and poisons electrocatalysts at the cathode.[8] Furthermore, with an increase in operation temperature, the proton conductivity of the Nafion membrane is depleted excessively due to dehydration of the membrane.[9,10]

It has been realized that operation of PEMFCs at elevated temperatures (>100 °C) under reduced humidification or anhydrous conditions will have significant advantages, such as increased activity of electrocatalysts and the concomitant reaction kinetics, simplification of the water and heat management system of the PEMFC, and enhanced tolerance to CO poisoning generated by the fuel oxidation reaction.[9,11,12] Consequently, there has been considerable interest in the development of alternative PEM materials that retain high proton conductivities at elevated temperatures. Phosphoric acid (PA), H_3PO_4, exhibits effective proton conductivity, even in the anhydrous form, with a conductivity of 0.568 S cm^{-1} for PA at 150 °C due to its unique proton conduction mechanism by self-

Received: August 19, 2013
Accepted: October 14, 2013
Published: October 14, 2013

ionization and self-dehydration.[13] PA also has a high boiling point (boiling point of H_3PO_4 85 wt % is ca. 154 °C). Accordingly, a new class of composite membranes, "acid-based polymer membranes", has been developed based on PA. A number of basic polymers have been tested as acid-based electrolytes, such as PEO,[14] PVA,[15] polyacrylamide,[16,17] and Nylon.[18] However, all of the above-mentioned acid−polymers blends exhibit poor proton conductivities < 10^{-3} S cm^{-1} at room temperature. Savinell et al. reported on the incorporation of phosphoric acid into Nafion, yielding a conductivity of 5 × 10^{-2} S cm^{-1} at 150 °C.[19] The most successful membrane to date for use in high-temperature PEMFCs is the PA-doped polybenzimidazole (PBI/PA) membrane.[20−26] The proton conductivity of the PBI/PA composite membrane was found to depend on the acid doping level, relative humidity (RH), and temperature. A high proton conductivity of 6.8 × 10^{-2} S cm^{-1} at 200 °C and 5% RH with a H_3PO_4 doping level of 5.6 (mole number of H_3PO_4 per repeat unit of PBI) has been reported for the PBI/PA membranes.[27] Xiao et al.[28,29] synthesized pyridine-based PBI, using polyphosphoric acid (PPA) as both the solvent and polycondensation agent, achieving a high proton conductivity of ∼0.2 S cm^{-1} at 200 °C. Despite the high conductivity of the PBI/PA-based membrane, its mechanical stability is problematic due to the high swelling of the membrane under humidified conditions. Dai et al. reported a swelling ratio in the thickness direction of PA-doped PBI membranes of 50−175% as the acid doping level rises from 2 to 6.[30] Kumbharkar et al. also demonstrated that the swelling ratio in volume was as high as 200−700% as the acid doping level was raised to 20.[31] It is evident that this high swelling ratio is detrimental to the structural stability of the membrane in an operational fuel cell. Also, the leaching of phosphoric acid from the membrane during operation of PEMFCs is an unresolved issue with PA-doped PBI membranes.

A new strategy involves the adoption of dimensionally stable meso- and nanoporous materials with incorporation of the proton conducting carrier (i.e., PA) as a new type of high-temperature PEM for fuel cells. Yamaguchi et al.[32] reported the development of a proton conductive composite based on impregnating and filling a porous polymeric framework with proton conductive dopants. This type of structure provided good mechanical stability, which led to reduced fuel crossover in the fuel cell.[33,34] Inorganic materials, such as mesoporous silica,[35] mesoporous aluminosilicate,[36] phosphate composites,[37−40] and P_2O_5−SiO_2 glass,[41,42] have also been applied as a support matrix in PEM applications. Mesoporous silicas with a tunable mesoporous structure, high specific surface area, nanosized channels or frameworks, and an ordered and interconnected internal structure are particularly attractive for applications in PEMs operated at elevated temperatures. Munakata et al.[43] reported that the proton conductivity of a macroporous silica/AMPS composite membrane was improved from 1 × 10^{-2} to 2.6 × 10^{-2} S cm^{-1} when a silica host with a smaller pore size was utilized. We have also found that a reduction in pore size of the mesoporous silica host from 12.1 to 5.0 nm led to an enhancement in the proton conductivity of an HPW (phosphotungstic acid)−mesoporous silica nanocomposite membrane from 4.9 × 10^{-2} to 6.8 × 10^{-2} S cm^{-1} at room temperature.[44] Surface modification of mesoporous silica with ionic groups, such as sulfonic acid,[45−47] protic ionic liquid,[48] and phosphoric acid,[49,50] has also been reported to yield enhanced proton conductivity. However, the ionic conductivity of surface-modified mesoporous silica depends strongly on the relative humidity (RH).[48,51] For example, Mishra et al.[48] showed that the proton conductivity of ionic liquid modified mesoporous silica decreased from ∼0.28 to 0.055 S cm^{-1} when the RH decreased from 90% to 30 % at 90 °C.

Furthermore, hot-pressing with the assistance of binders is a common technique to fabricate membrane electrolytes for inorganic proton conductors.[35,48,51,52] However, the mechanical strength of a hot-pressed membrane is low. For example, the mechanical strength of hot-pressed HPW-functionalized *meso*-silica is as low as 5 MPa.[53] The weak mechanical strength is a significant technological barrier for the wide and practical application of inorganic proton conductor-based membranes for fuel cells. Here, we present the synthesis and characterization of a novel proton exchange membrane based on PA-functionalized sintered mesoporous silica (PA-*meso*-silica) for PEMFCs at elevated temperatures (above 150 °C) and under anhydrous conditions. The PA-*meso*-silica materials combine physicochemical attributes that are not available in previously reported membranes based on polymeric, inorganic, or composite solids. In particular, presintering of *meso*-silica membranes led to a dimensionally stable membrane. These membranes have robust mesostructures that can be functionalized to produce desirable PA retention and proton conduction properties.[54] Additionally, the presintered silica membranes have a much higher mechanical strength, as compared to the hot-pressed *meso*-silica membranes. Such PA-*meso*-silica PEMs exhibit excellent proton conductivity along with high performance based on a hydrogen fuel cell under anhydrous conditions.

2. EXPERIMENTAL SECTION

2.1. Synthesis of Sintered *meso*-Silica/Phosphoric Acid (PA) Nanocomposites. The synthesis of mesoporous silica with $Ia\bar{3}d$ symmetries utilized procedures reported in the literature.[55−57] Pluronic surfactant P123 and hydrochloric acid were dissolved in deionized water. After complete dissolution, butanol was added, and after stirring for 1 h at 45 °C, tetraethylorthosilicate (TEOS, Sigma-Aldrich) was added. The mixture was stirred vigorously at 45 °C for 24 h and subsequently aged at 100 °C for 24 h; the mixture was dried at room temperature. The resultant powder was calcined at 650 °C for 6 h to remove the template with N_2 as a protective gas at temperatures below 200 °C. The as-prepared *meso*-silica powder was pressed in a die to form *meso*-silica discs, followed by sintering at a temperature range of 550−850 °C. The sintered *meso*-silica discs were subsequently polished and impregnated in an 83 wt % PA solution for 24 h, forming PA-functionalized *meso*-silica membranes. The PA-*meso*-silica disc had a diameter of 3.8 cm and a thickness of ∼500 μm. Figure 1 shows the optical photograph of a sintered *meso*-silica disc and a PA-*meso*-silica disc membrane. The pure *meso*-silica disc was white in color and

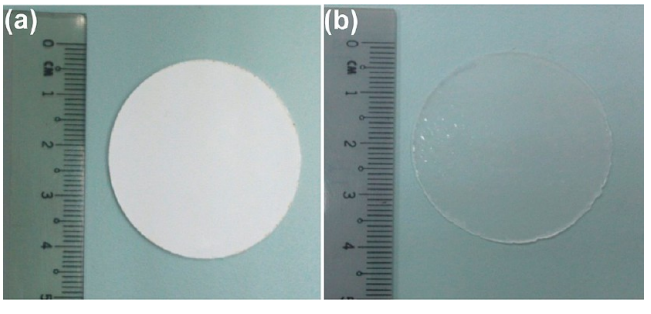

Figure 1. Optical pictures of (a) a *meso*-silica disc sintered at 650 °C for 20 h and (b) a PA-*meso*-silica disc membrane with 28 wt % PA.

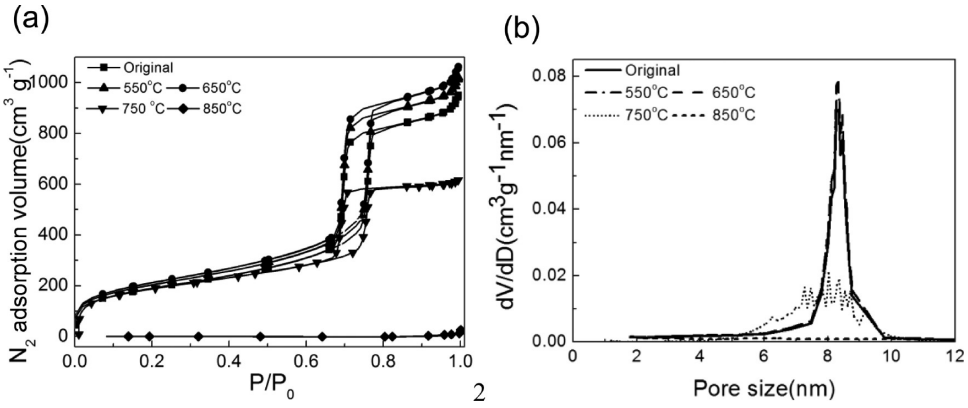

Figure 2. (a) N_2 absorption isotherms and (b) pore size distribution of *meso*-silica disc membrane sintering at various temperatures.

changed to optically transparent after functionalizing with PA. The appearance and color of PA-*meso*-silica remained relatively constant after soaking in phosphoric acid for more than 8 months, which suggests excellent mechanical and chemical stability for the sintered *meso*-silica structure.

For the purpose of comparison, conventional porous silica powders were prepared using TEOS as silica source and synthesized in a hydrothermal reactor under the same temperature and pH value to that of mesoporous silica, but without the use of Pluronic surfactant P123. The conventional porous silica was white in color and very fine. Its surface area was 120 $m^2\ g^{-1}$ from the BET result. The porous silica powder was pressed and sintered at 650 °C for 20 h, followed by impregnation in a 83 wt % PA solution for 24 h. The PA-functionalized sintered conventional porous silica membrane was denoted as PA-porous-silica.

2.2. Structural Characterization. Small-angle X-ray scattering (SAXS) spectra were carried out at the SAXS/WAXS beamline at the Australian Synchrotron. All measurements were undertaken using an X-ray wavelength of 1.127 Å or beam energy of 20 keV at a camera length set at 0.959 m. The scattering vector q has units of $Å^{-1}$ and is given by

$$q = 4\pi\frac{\sin\theta}{\lambda} \tag{1}$$

where θ is the scattering angle and λ is the radiation wavelength.

Nitrogen adsorption/desorption isotherms were measured using a Micromeritics ASAP Tristar II 3020 system. The samples were degassed at 300 °C overnight under a nitrogen flow. Specific surface area was calculated using the Brunauer–Emmett–Teller (BET) method. The total pore volumes were estimated from the adsorbed amount at the relative pressure of P/P_0 = 0.95, and the pore size distributions were obtained from the adsorption branch of the isotherms by using the nonlinear density functional theory (NLDFT) method. Transmission electron microscopy (TEM) images were obtained using a JSM-2100F JEOL electron microscope equipped with an EDX-detector (Noran Instr.) and operated at 200 kV with a cold-field emission source. Thermal gravimetric analysis (TGA) was carried out on a TG/DTA Q500 from 30 to 500 °C at a heating rate of 10 °C min^{-1} in a nitrogen flow of 40 mL min^{-1}. Fourier transform infrared (FTIR) absorption spectra of the PA/*meso*-silica composite membranes were recorded with a JASCO FTIR-Q250 spectrometer (spectral range of 4000–200 cm^{-1}, 50 scans, and a resolution of 1 cm^{-1}). An atomic force microscope (AFM, Nanoscope IIIA, Digital Instruments) was used to examine the surface morphology and roughness of the *meso*-silica sintered at 650 °C for different times. The AFM was conducted by tapping mode.

2.3. Determination of Weight Increase, Water Uptake, Swelling Ratio, Wettability, and Mechanical Properties. The doping level and water uptake of PA-*meso*-silica membranes were determined by measuring the weight differences between undoped and vacuum-dried PA-*meso*-silica membranes. First, the *meso*-silica membrane was dried under vacuum at 120 °C overnight and the dry weight (W_{dry}) was recorded. Consequently, the dry membranes were immersed in H_3PO_4 solution (83 wt %). After 72 h, the membranes were taken out and dried with tissue paper, and the wet weight, W_{wet}, was measured. The PA-doped membrane were dried again at 120 °C under vacuum for 24 h and weighed again, which gave the weight of the *meso*-silica with PA, W_{acid}

$$\text{Weight increase (wt \%)} = \frac{W_{wet} - W_{dry}}{W_{dry}} \times 100\% \tag{2}$$

$$\text{Water uptake (wt \%)} = \frac{W_{wet} - W_{acid}}{W_{dry}} \times 100\% \tag{3}$$

$$\text{Swelling ratio (\%)} = \frac{l_{wet} - l_{dry}}{l_{dry}} \times 100\% \tag{4}$$

where l_{dry} and l_{wet} are the thickness of dried and wet membranes, respectively.

The wettability of a solid surface depends on both the surface energy and the surface roughness and, with a certain kind of liquid on the solid surface, the wettability is usually represented by the static contact angle. The static contact angle is the angle at the solid, liquid, and gas interface. The static contact angle (θ_c) represents the angle measured at the liquid/gas interface on the solid surface from the liquid side. When a liquid water droplet on a solid surface has a static contact angle of less than 90°, this is defined as a hydrophilic surface, whereas other contact angles represent a hydrophobic surface.

The mechanical strength of the composite membranes was evaluated using an Instron model 5948 Micro Tester at room temperature in accordance with ASTM Standards. The tensile strengths were measured using the Bluehill Materials Testing Software with a programmed elongation rate of 10 $\mu m\ s^{-1}$. The ultimate tensile strength of the membrane was calculated using the average thickness of the specimen and the maximum breaking load.

2.4. Single Cell Assembly, Measurements of Conductivity, and Cell Performance. The proton conductivity of the PA-*meso*-silica membrane disc was measured using a four-probe method and electrochemical impedance spectroscopy (EIS) with a PGSTAT30/FRA, (Autolab, Netherlands) potentiostat in the frequency range of 1 Hz to 1 MHz and the temperature range of 80–220 °C in the absence of external humidification. For the purposes of comparison, the Nafion 117 membrane and PA-porous-silica membranes were also measured.

The membrane–electrode assembly (MEA) based on the PA-*meso*-silica disc membrane was assembled for the single cell test. The PA-*meso*-silica disc was 3.8 cm in diameter and ~500 μm in thickness. A mixture of PtRu/C catalyst (40% Pt and 20% Ru on Vulcan XC-72R Carbon, Johnson Matthey), Nafion solution (5 wt % in a mixture of aliphatic alcohols, Sigma Aldrich), and isopropyl alcohol (Sigma-Aldrich) was sprayed onto a carbon gas diffusion layer (Toray Graphite Paper, TGPH-120, 40% wet-proofed, E-TEK, Inc.) by air-brushing until a platinum loading of 3 mg cm^{-2} was achieved for the

Table 1. Textural Parameters of Mesoporous Silica Sintered at Different Temperatures

samples	S_{bet} (m^2 g^{-1})	pore vol (cm^3 g^{-1})[a]	pore size (nm)[b]	wall thickness (nm)[c]
meso-silica (before sintering)	913 ± 8	1.146	8.2	5.0 ± 0.2
meso-silica-550 °C	936 ± 10	1.238	8.2	4.8 ± 0.2
meso-silica-650 °C	948 ± 12	1.312	8.2	4.2 ± 0.2
meso-silica-750 °C	522 ± 4	0.488	8.0	3.9 ± 0.6
meso-silica-850 °C	87 ± 3	0.131	N.A.	N.A.

[a]Cumulative pore volume. [b]Calculated from the adsorption branch of the isotherms based on the NLDFT method. [c]Calculated from BET results.

anode. The same procedure was used for the cathode with a Pt loading of 2 mg cm^{-2} (60% Pt on Vulcan XC-72R Carbon, Johnson Matthey). The carbon paper electrodes with the sprayed Pt catalyst layer were placed onto the PA-*meso*-silica membrane without hot-pressing. The electrode area was 4.0 cm^2. The relative humidity (RH) of the fuel cell was controlled by a PEMFC test station (FCATS-G050, Greenlight, Canada) and was measured in situ using an HM141 humidity sensor (Vaisala, USA). The cell performance was measured in a H_2 flow of 100 mL min^{-1} and the O_2 flow of 40 mL min^{-1}. No back pressure control was utilized in both sides of the cell in this study.

3. RESULTS AND DISCUSSIONS

3.1. Effect of Sintering Temperature and Time on Silica Mesoporous Structure. The porosity of original and sintered *meso*-silica was probed with nitrogen sorption measurements. Figure 2 shows the N_2 sorption isotherms and corresponding pore size distribution. The N_2 sorption isotherms feature typical type-IV associated with a distinct step at a relative pressure of ~0.7 that is attributed to nitrogen condensation in a narrow size distribution of mesopores for all samples except for the disc sintered at 850 °C. Further analysis indicated H1 hysteresis loops for the mesoporous silica, which suggested a cylindrical pore shape for this textural structure.[58,59] This indicates that the ordered structure of mesoporous silica is stable at a sintering temperature of 650 °C and becomes disordered at sintering temperatures of 750 °C and higher. Our previous work showed that differences in pore shape lead to varied impregnation behavior, and a cylindrical pore seems to favor impregnation over an ink-bottle pore shape.[60] The *meso*-silica with the $Ia\bar{3}d$ structure that has both cylindrical pores and the largest pore volume among the various *meso*-silica symmetries was subsequently utilized in this work.

The textural parameters of the mesoporous silica and the corresponding samples sintered at different temperatures are listed in Table 1. The analysis of the N_2 adsorption isotherms with the Brunauer–Emmett–Teller method gave surface areas of ~913 m^2 g^{-1} for mesoporous silica without sintering, significantly higher than ~120 m^2 g^{-1} measured on conventional porous silica synthesized without the use of a surfactant template. Despite the slight increase in adsorption volume and specific surface area, the *meso*-silicas sintered in the temperature range of 550–650 °C indicate similar N_2 sorption isotherms to that of the original *meso*-silica, as illustrated in Figure 2a. No significant change in pore size distribution was observed as the pore sizes of *meso*-silica, *meso*-silica sintered at 550 °C, and *meso*-silica sintered at 650 °C distributed evenly around 8.2 nm (Figure 2b). The mesostructure of *meso*-silica started to collapse at 750 °C, which is indicated by a significant decrease in the pore volume and specific surface area, also noting that the pore size distribution was scattered in the range of 7.2–9.4 nm. The sintered-*meso*-silica membrane lost its "mesoporous" structure at a sintering temperature of 850 °C. Accordingly, in subsequent work, 650 °C was used as the sintering temperature of *meso*-silica discs.

Figure 3 shows the SAXS data for the sintered mesoporous silica before and after PA functionalization. The sintered sample

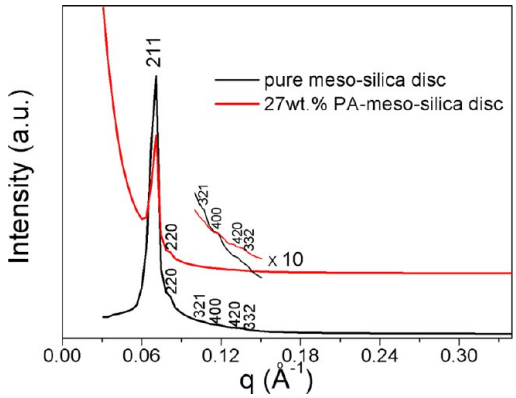

Figure 3. Small-angle X-ray scattering patterns of the mesoporous silica disc sintered at 650 °C and PA-*meso*-silica with 28 wt % PA. The inset is the enlarged scattering patterns indexed to 321, 400, 420, and 332.

shows well-resolved scattering peaks that are characteristic of the $Ia\bar{3}d$ symmetry,[61] suggesting the successful formation of the well-ordered $Ia\bar{3}d$ mesoporous structure. After impregnation with PA, there was a significant diminution in the relative intensities of the 211, 220, 321, 400, 420, and 431 SAXS peaks of the $Ia\bar{3}d$ structure. However, the position of the scattering peaks for PA-*meso*-silica composites remains similar to that of the corresponding *meso*-silica hosts. This infers that the symmetry and dimensional properties of the *meso*-silica host have been preserved during PA impregnation. The lattice parameter of the sintered *meso*-silica, α, is 21.72 nm, and α is 21.67 nm following impregnation by PA. A likely explanation for the decrease in relative intensities of SAXS scattering peaks is that impregnation of the silica mesopores by PA molecules reduces the X-ray scattering contrast between the walls and pores in the *meso*-silica structure, leading to a diminished scattering of X-rays in the SAXS measurements.

The purpose of the sintering of the mesoporous silica membrane is to integrate the *meso*-silica membrane into an air-tight, crackless separator that provides excellent resistance to fuel crossover and high mechanical strength during fuel cell operation. Furthermore, it is essential to improve contact at the interface between the membrane and catalytic electrodes, which requires smooth and pinhole-free surfaces in the membrane. The surface roughnesses of *meso*-silica sintered for different times at a constant temperature of 650 °C are presented in Figure 4. It is evident in the AFM micrographs of Figure 4 that pinholes with diameters of ~0.5 μm are present in the original or unsintered membrane. The surface roughness of *meso*-silica membrane has been reduced significantly after sintering for 10 h, and no pinholes in the micrometer size range are evident on

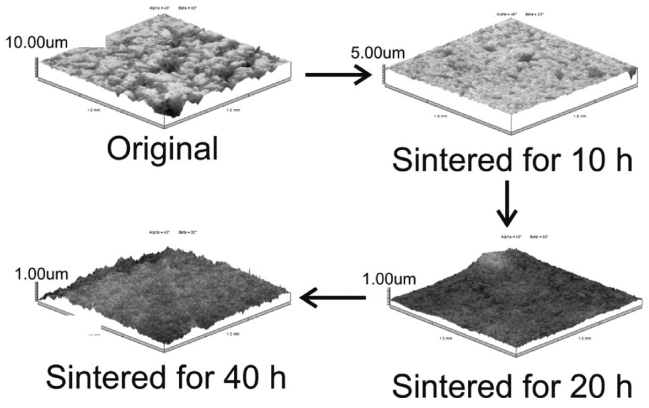

Figure 4. AFM images of surface morphology and roughnesses of mesoporous silica membrane sintered at 650 °C from 10 to 40 h.

the membrane surface after 20 h of sintering. The *meso*-silica membranes sintered at 650 °C for 20 h were subsequently selected as matrix materials for further use in fuel cell and other tests.

3.2. Mechanical Properties, Water Uptake, and Wettability. The mechanical strength of sintered *meso*-silica membranes was 51 MPa, significantly higher than 19 MPa measured on hot-pressed *meso*-silica samples under identical conditions. However, the elongation at breaking is ∼1%, indicating that the sintered *meso*-silica membrane is still brittle. The water uptake and swelling ratio of *meso*-silica and PA-*meso*-silica disc membranes are presented in Table 2, noting that the water uptake and swelling of Nafion 117, original *meso*-silica, and PBI/PA membranes are provided for comparison. The results show that PA-*meso*-silica disc membranes have excellent water retention and negligible swelling, which are highly beneficial in PEMFC applications.

Table 2. Weight Increase, Water Uptake, and the Swelling Ratio of Various Membrane Materials

membrane	weight increase (wt %)	water uptake (wt %)	swelling ratio in thickness (%)
Nafion 117	23 ± 2	21 ± 2	18 ± 3
meso-silica	28.2 ± 4	26.6 ± 4.3	negligible
PBI/PA	30−140	35−210	50−700
PA-*meso*-silica	35.6 ± 2.2	9.5 ± 2.1	negligible
aged PA-*meso*-silica	37.0 ± 2.6	11.0 ± 3.2	negligible

The wettability of PA-*meso*-silica membranes was studied using contact angles on the PA-*meso*-silica membrane before and after aging, and the results are presented in Figure 5. The Nafion 117 membrane, which is a typical hydrophilic material, was also measured for comparision. The incorporation of phosphoric acid into the interior pore walls of mesoporous silica results in more surface hydroxyl functional groups, leading to improved wettability. After soaking in 85 wt % phosphoric solution for 8 months, a decrease in the water contact angle can be observed, suggesting that both the inner and the outside surface of the mesoporous framework become more hydrophilic. The contact angles of the measured membrane surfaces are presented in Table 3.

Table 3. Contact Angle of Nafion 117 Membrane, PA-*meso*-silica Membrane, and Aged PA-*meso*-silica Membrane

various proton conductive membrane	contact angle (left) (deg)	contact angle (right) (deg)	contact angle (mean) (deg)
Nafion 117	57.81 ± 2.89	52.54 ± 2.53	54.62 ± 2.71
PA-*meso*-silica	54.84 ± 2.04	57.25 ± 2.12	56.05 ± 2.08
aged PA-*meso*-silica	44.74 ± 2.02	44.75 ± 1.96	44.75 ± 1.99

3.3. Morphology of Sintered *meso*-Silica Disc Membrane. Figure 6 shows FESEM images of sintered *meso*-silica

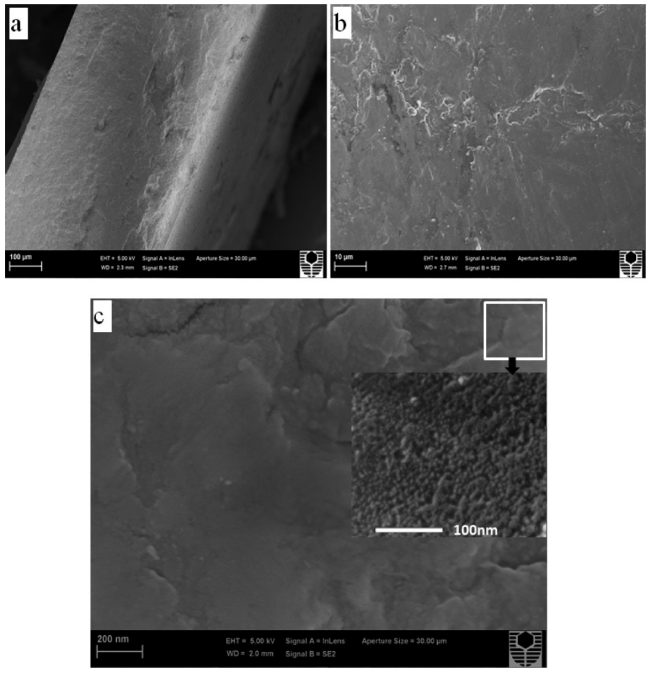

Figure 6. FESEM images of sintered *meso*-silica membranes: (a) overview of the cross section, (b) cross section, and (c) surface.

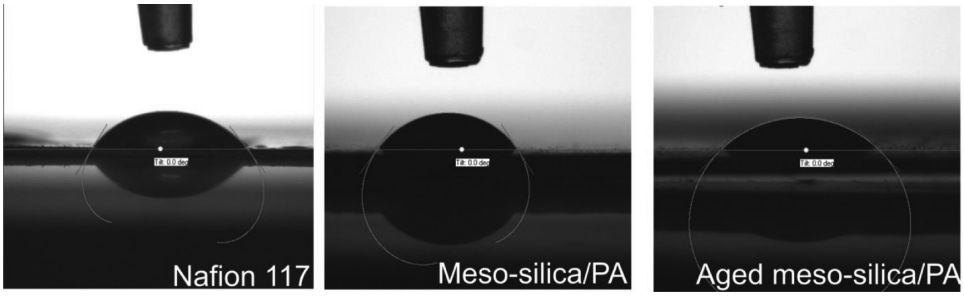

Figure 5. Contact angle of water drop on the surface of Nafion 117, PA-*meso*-silica membrane, and PA-*meso*-silica membrane aged for 8 months.

membranes. The membrane was characterized by closely packed silica particles along with a uniform texture when viewed at low magnitude, and there are very few, if any, pinholes or cracks at the micrometer scale evident on the cross section of the membrane (Figure 6a,b). High-magnification images indicated that the uniform distribution of mesopores was evident across the surface and throughout the cross section of the *meso*-silica membrane (Figure 6c).

Figure 7 shows TEM images with the cubic bicontinuous structure ($Ia\bar{3}d$). The *meso*-silica structure is characterized by a

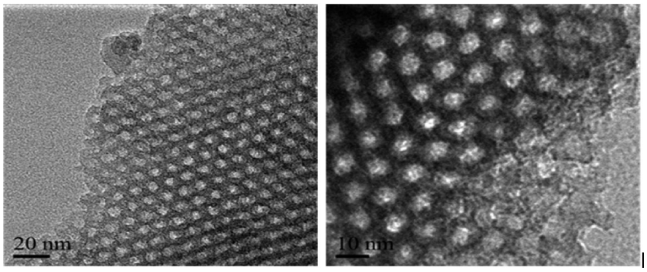

Figure 7. TEM images of mesoporous silica with cubic bicontinuous structure viewed from the [111] direction.

hexagonal arrangement of parallel or interconnected pore channels. The mesoporous channels are white in color, and the siliceous walls are in grey color. The TEM images of mesoporous silica show regular arrays of mesopores, which, after indexing the fast-Fourier transform (FFT) patterns, can be assigned to the [110] and [111] directions of the $Ia\bar{3}d$ symmetries, respectively.

3.4. TGA and FTIR Analysis. The thermal properties of mesoporous silica based membranes have been investigated using TGA (see Figure 8). In the case of *meso*-silica with a

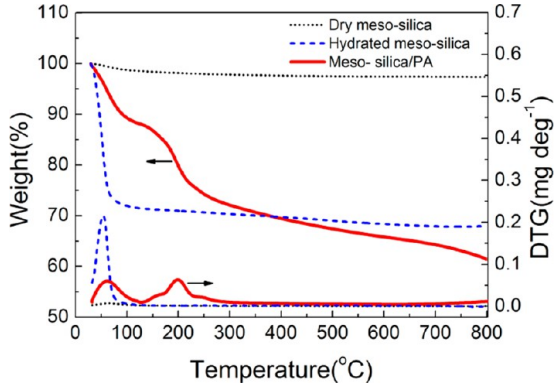

Figure 8. Thermogravimetic analyses (TGA) of dry *meso*-silica membrane, fully hydrated *meso*-silica membrane, and PA-*meso*-silica membrane.

structural symmetry of $Ia\bar{3}d$, the weight loss occured mainly at a temperature of 60 °C, which is attributed to the dehydration of adsorbed water. The dry *meso*-silica membrane contains ca. 1.2 wt % water, compared to ca. 26 wt % for the fully hydrated mesoporous silica. The relatively high hydration capacity results from the large pore volume of the *meso*-silica membrane.

On the other hand, the PA-*meso*-silica membrane exhibited two distinct weight loss processes in the temperature range of 30–800 °C. The first weight loss commenced at ambient temperature up to 100 °C, which is mainly attributable to absorbed water from doping using a phosphoric acid solution and unbound phosphoric acid on the membrane surface. The second weight loss at about 200 °C is assigned to the volatilization of phosphoric acid. The high doping level of H_3PO_4 in PA-*meso*-silica is reflected in the total weight loss of 38% at 800 °C, which is ascribed to the dehydration of doping phosphoric acid. The high doping level reflects a large pore volume in the *meso*-silica membrane.

It is evident in the FTIR spectra of mesoporous silica of Figure 9a that the weak band at 1612 cm^{-1} is due to the OH bending mode of adsorbed water, with the broad band at 801 cm^{-1} due to the characteristic vibrations of Si–O–Si.[62] The FTIR spectra of H_3PO_4-doped *meso*-silica before and after aging showed the characteristic peaks of the phosphoric acid moiety, viz., δP═O and δP–O appearing at 951 and 894 cm^{-1}, respectively. The coupled bands at 1050 and 765 cm^{-1} are assigned to in-plane and out-of-plane bending modes of P–O–H, respectively.[63,64] These FTIR spectra are a clear indicator of the success of the PA immobilization process. The spectra also observed a significant shift in the OH bending mode of adsorbed water from 1612 to 1634 cm^{-1}, which results from the protonation of water within the membrane.

The Raman scattering spectra of *meso*-silica, PA-*meso*-silica, and aged PA-*meso*-silica membranes are presented in Figure 9b. By comparison to the spectrum of an undoped *meso*-silica membrane, there are significant differences in the spectra of the PA-*meso*-silica membranes. The very strong bands that appear at 900 cm^{-1} may be ascribed to the P–O stretching in H_3PO_4, while the OH stretching yields another strong band at 2026 cm^{-1}. The bands at 376 and 488 cm^{-1} are assigned to the vibrational mode of P–O in the phosphate group, which is indicative of the formation of P–O–P and/or Si–O–P bonds in the hybrids. The intensity of the peaks in the Raman spectrum of the aged PA-*meso*-silica samples is significantly intense than that in the freshly prepared PA-*meso*-silica. This is consistent with the FTIR results. As shown in Figure 9a, it is also noted that the peaks assigned to phosphate at 951 and 894 cm^{-1} reverse in relative intensity before and after aging. The increase in the intensity of the vibration mode of δP–O may indicate the increased formation of P–O–P or Si–O–P bonds in the hybrids, suggesting that aging has a significant effect on the PA-*meso*-silica membranes.

3.5. Proton Conductivity and Cell Performance. The proton conductivity of the PA-*meso*-silica composite was measured, and the results were averaged over at least three different samples. The conductivity of the commercial Nafion 117 membrane was also measured and reported for comparison. It can be seen in Figure 10 that the PA-*meso*-silica membranes show quite promising conductivities of 4×10^{-3} to 6×10^{-2} S cm^{-1} in the temperature range of 80–225 °C, which is about 1 order of magnitude higher than the conductivity of the PA-functionalized sintered conventional porous silica (PA-porous-silica) composite membrane (5×10^{-5} to 3×10^{-3} S cm^{-1}). For the proton conduction of the PA-*meso*-silica membrane, the activation energy, E_a, of 18.2 kJ mol^{-1}, is much lower than 32.5 kJ mol^{-1} for the PA-porous-silica membrane. The much lower conductivity and higher activation energy for the PA-porous-silica membrane are most likely due to the low specific surface area (120 m^2 g^{-1}) and randomly distributed micropores typically associated with sol–gel derived silica materials. Additionally, the PA-*meso*-silica membranes exhibited superior conductivity without humidification compared to Nafion 117 and PBI/PA membranes.

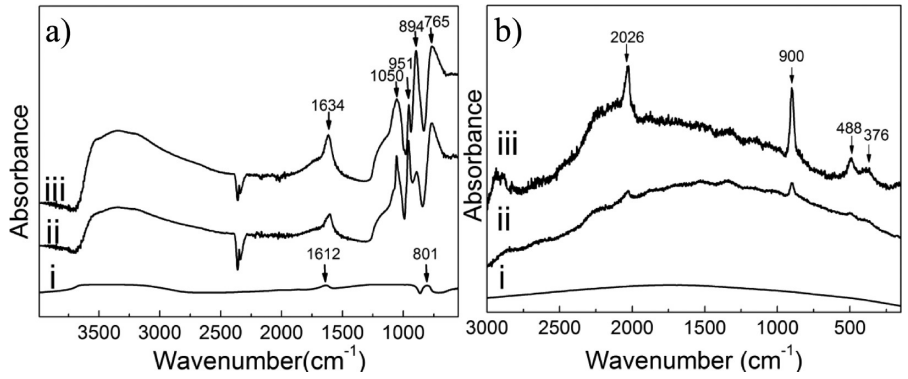

Figure 9. FTIR spectra (a) and Raman scattering spectra (b) of (i) *meso*-silica membrane, (ii) PA-*meso*-silica membrane, and (iii) PA-*meso*-silica membrane aged in phosphoric acid for 8 months.

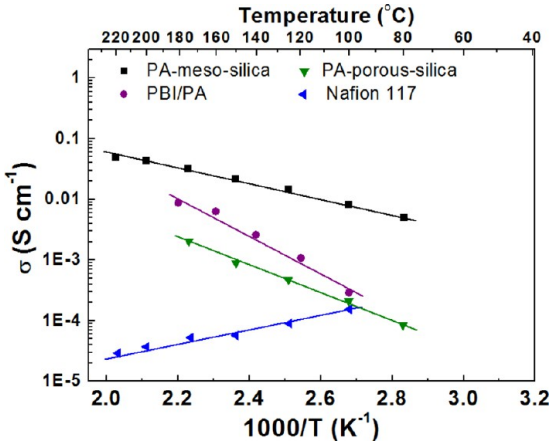

Figure 10. Conductivity as a function of (inverse) test temperature without external humidification control (black square) PA-*meso*-silica membrane, (green triangle) PA-porous-silica membrane, (purple circle) PBI/PA membrane from ref 65, and (blue triangle) Nafion 117 membrane.

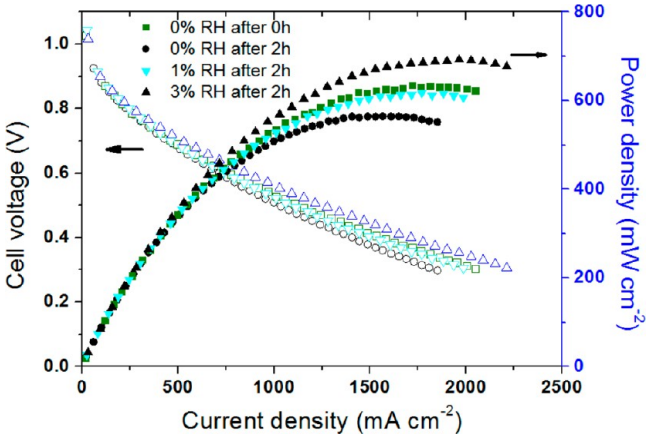

Figure 11. Polarization and power density of a single cell employing a PA-*meso*-silica membrane in H_2/O_2 at 190 °C in H_2/O_2 (1/1 atm). The numbers in the figure are the RHs of hydrogen gas.

Without humidification, the conductivity of Nafion 117 dropped significantly from 1.8×10^{-4} to 2.2×10^{-5} S cm^{-1} as the temperature was raised from 100 to 220 °C. Conversely, the PBI/PA membrane was highly functional within the temperature range of 100−180 °C, although the PBI/PA membrane exhibited a lower conductivity of 2.9×10^{-4} to 8.8×10^{-3} S cm^{-1} and a higher activation energy, 34.7 kJ mol^{-1}, in the absence of external humidification.[65]

To demonstrate the applicability of the PA-*meso*-silica composite membrane as a proton-conducting membrane in PEMFCs, a single cell was assembled with a PA-*meso*-silica membrane that is 220 μm thick, which was coupled to a Pt/C catalyst as the anode and cathode. The effective area of the cell was 4 cm^2. Significantly, the hydrogen crossover current of the composite membrane was found to be 12 mA cm^{-2} at 150 °C, which indicates a very good membrane resistance to H_2 crossover.

Figure 11 illustrates the influence of water content on the performance of a PA-*meso*-silica composite membrane based cell at a temperature of 190 °C. The open-circuit voltage (OCV) of the PEM fuel cell in H_2/O_2 at 190 °C is 1.03 V, close to that of typical single cells assembled with Nafion membranes below 80 °C. This provides further credence for the PA-*meso*-silica membrane acting as a very good barrier to hydrogen crossover. Furthermore, the initial polarization curve was obtained under anhydrous conditions (0 h at 0% RH) and achieved a peak power density of 632 mW cm^{-2} at 190 °C and a current density of 0.5 A cm^{-2} at a cell voltage of 0.7 V. The power output of the PA-*meso*-silica cells is quite high when compared to results on other inorganic membrane based fuel cells, such as In^{3+}-doped SnP_2O_7 (264 mW cm^{-2} at 250 °C),[66] a CsH_2PO_4-based electrolyte (48.9 mW cm^{-2} at 235 °C),[67] and HPMo/HPW-doped glass electrolytes (32 mW cm^{-2} at 29 °C).[68] As reported by Zhang et al.,[69] the peak power density of a Nafion 112 membrane H_2/O_2 fuel cell was 572 mW cm^{-2} at 120 °C/100% RH. The corresponding peak power density of the PA-*meso*-silica membrane is relatively high at higher temperature and free of the complications associated with humidity and pressure control in a Nafion 112 membrane fuel cell. Preliminary data showed that the cell performance is very stable during the initial test period of ∼70 h under test conditions at 400 mA cm^{-2} and 160 °C in H_2/O_2,[54] indicating a good stability of PA impregnated within the mesoporous silica matrix structure. Nevertheless, similar to the PBI/PA hybrid membranes, PA could leach from the mesoporous silica matrix. Thus, it is important to investigate the intrinsic relationship between the mesoporous structure of the silica matrix and the stability and leaching behavior of the impregnated PA.

Later, the data were collected at intervals with a further reduction in the PEMFC performance noted, until a steady-state condition was reached after 2 h. A small, but noticeable, decrease in power density (viz., 570 mW cm^{-2}) was observed

after operating in an anhydrous environment for 2 h, which is mainly attributed to a loss in membrane conductivity. This effect is probably due to water loss induced by acid dimerization. At elevated temperatures, PA starts to dehydrate, which occurs in multiple stages, the first two of which are given below:

$$\text{First stage: } 2H_3PO_4 \leftrightarrow H_4P_2O_7 + H_2O\uparrow \quad (5)$$

$$\text{Second stage: } H_4P_2O_7 + H_3PO_4 \leftrightarrow H_5P_3O_{10} + H_2O\uparrow \quad (6)$$

The equilibrium concentrations of these reversible reactions are dependent on temperature and relative humidity, noting that the dimerized PA products are reported to possess a significantly lower proton conductivity than PA.[70] This is also demonstrated by the fact that the performance of the PA-*meso*-silica cell increases with the water content. To illustrate this point, 1% RH was introduced into the hydrogen stream and the system was stabilized for 2 h before taking the first measurement. As shown in Figure 11, a significant enhancement in the peak power density was observed. When the RH increased to 3%, the maximum power density is ~700 mW cm^{-2}, presumably a signal of the increase in membrane conductivity. The increase in the power output with humidity of the PA-*meso*-silica membrane cells is consistent with that reported for PA/PBI membrane cells.[27] Note that the cell resistance (at 190 °C) of the PA-*meso* silica membrane was found to be 0.14, 0.13, and 0.125 Ω cm^2 for 0%, 1%, and 3% RH in hydrogen, respectively.

4. CONCLUSIONS

In this work, we have successfully prepared novel inorganic proton exchange membranes based on phosphoric acid (PA)-functionalized and sintered mesoporous silica with a 3D symmetry of $Ia\bar{3}d$. After sintering at 650 °C, SAXS and N_2 adsorption isotherm data indicated that presintering of *meso*-silica preserved the mesoporous structure, providing an excellent ordered porous support for impregnation by PA. Most importantly, this high degree of ordering and the presence of nanochannels are critical to the retention of PA (other acids as well) within the structure. The surface roughness, water uptake, and wettability, as well as water contact angle of *meso*-silica membrane were also investigated. The PA-functionalized presintered *meso*-silica electrolytes displayed a high proton conductivity and thermal stability at elevated temperature in the absence of external humidification, as compared with commercial Nafion 117 and PBI/PA membranes. The PA-*meso*-silica membrane achieved high proton conductivities of 0.005 and 0.05 S cm^{-1} at 80 and 220 °C, respectively, with an activation energy of 18.2 kJ mol^{-1}. The performance of the PEMFCs with a PA-*meso*-silica nanocomposite membrane achieved a maximum power density of 632 mW cm^{-2} in a H_2 fuel in the absence of external humidification at 190 °C. The good performance of the PEMFCs demonstrated that inorganic proton exchange membranes with high proton conductivities and stabilities can be realized in PA-*meso*-silica nanocomposites with 3D mesostructures. The cell performance and stability may be further improved through an optimization of the interfacial contact between the electrocatalytic layer and the inorganic membrane.

AUTHOR INFORMATION

Corresponding Author

*Tel: +61 8 9266 9804. Fax: +61 8 9266 1138. E-mail: s.jiang@curtin.edu.au.

Notes

The authors declare no competing financial interest.

ACKNOWLEDGMENTS

The project is supported by the Australian Research Council (DP120102325), Australia, and the Major International (Regional) Joint Research Project of the National Natural Science Foundation of China (51210002). The SAXS measurements were carried out on the SAXS beamline at the Australian Synchrotron (AS), Victoria, Australia. Dr. Nigel Kirby at the AS is also thanked for assistance with the SAXS experiments. The authors acknowledge the facilities and scientific and technical assistance of the Curtin University Electron Microscope Facility and Curtin X-Ray Laboratory, both of which are partially funded by the University, State and Commonwealth Governments.

REFERENCES

(1) Devanathan, R. *Energy Environ. Sci.* **2008**, *1*, 101.
(2) Srinivasan, S.; Mosdale, R.; Stevens, P.; Yang, C. *Annu. Rev. Energy Environ.* **1999**, *24*, 281.
(3) Wang, Y.; Chen, K. S.; Mishler, J.; Cho, S. C.; Adroher, X. C. *Appl. Energy* **2011**, *88*, 981.
(4) Samms, S. R.; Wasmus, S.; Savinell, R. F. *J. Electrochem. Soc.* **1996**, *143*, 1498.
(5) Saito, M.; Arimura, N.; Hayamizu, K.; Okada, T. *J. Phys. Chem. B* **2004**, *108*, 16064.
(6) Jiang, S. P.; Tang, H. L. *Colloids Surf., A* **2012**, *407*, 49.
(7) Fuller, T. F.; Newman, J. *J. Electrochem. Soc.* **1992**, *139*, 1332.
(8) Arico, A. S.; Srinivasan, S.; Antonucci, V. *Fuel Cells* **2001**, *1*, 133.
(9) Li, Q. F.; He, R. H.; Jensen, J. O.; Bjerrum, N. J. *Chem. Mater.* **2003**, *15*, 4896.
(10) Thompson, E. L.; Capehart, T. W.; Fuller, T. J.; Jorne, J. *J. Electrochem. Soc.* **2006**, *153*, A2351.
(11) Zhang, J. L.; Xie, Z.; Zhang, J. J.; Tanga, Y. H.; Song, C. J.; Navessin, T.; Shi, Z. Q.; Song, D. T.; Wang, H. J.; Wilkinson, D. P.; Liu, Z. S.; Holdcroft, S. *J. Power Sources* **2006**, *160*, 872.
(12) Li, Q. F.; He, R. H.; Gao, J. A.; Jensen, J. O.; Bjerrum, N. J. *J. Electrochem. Soc.* **2003**, *150*, A1599.
(13) Gillespie, R. J.; Robinson, E. A. In *Nonaqueous Solvent Systems*; Waddington, T.C., Ed.; Academic Press: New York, 1965.
(14) Donoso, P.; Gorecki, W.; Berthier, C.; Defendini, F.; Poinsignon, C.; Armand, M. B. *Solid State Ionics* **1988**, *28-30*, 969.
(15) Petty-Weeks, S.; Zupancic, J. J.; Swedo, J. R. *Solid State Ionics* **1988**, *31*, 117.
(16) Rodriguez, D.; Jegat, C.; Trinquet, O.; Grondin, J.; Lassegues, J. C. *Solid State Ionics* **1993**, *61*, 195.
(17) Tanaka, R.; Yamamoto, H.; Shono, A.; Kubo, K.; Sakurai, M. *Electrochim. Acta* **2000**, *45*, 1385.
(18) Grondin, J.; Rodriguez, D.; Lassues, J. C. *Solid State Ionics* **1995**, *77*, 70.
(19) Savinell, R.; Yeager, E.; Tryk, D.; Landau, U.; Wainright, J.; Weng, D.; Lux, K.; Litt, M.; Rogers, C. *J. Electrochem. Soc.* **1994**, *141*, L46.
(20) Kawahara, M.; Rikukawa, M.; Sanui, K.; Ogata, N. *Solid State Ionics* **2000**, *136*, 1193.
(21) He, R. H.; Li, Q. F.; Bjerrum, N. J. *Chem. J. Chin. Univ.* **2005**, *26*, 2302.
(22) He, R. H.; Li, Q. F.; Jensen, J. O.; Bjerrum, N. J. *J. Polym. Sci., Part A: Polym. Chem.* **2007**, *45*, 2989.
(23) Lebaek, J.; Ali, S. T.; Moller, P.; Mathiasen, C.; Nielsen, L. P.; Kaer, S. K. *Int. J. Hydrogen Energy* **2010**, *35*, 9943.

(24) Ma, Y. L.; Wainright, J. S.; Litt, M. H.; Savinell, R. F. *J. Electrochem. Soc.* **2004**, *151*, A8.
(25) Wang, J. T.; Wainright, J. S.; Savinell, R. F.; Litt, M. *J. Appl. Electrochem.* **1996**, *26*, 751.
(26) Wainright, J. S.; Wang, J. T.; Weng, D.; Savinell, R. F.; Litt, M. *J. Electrochem. Soc.* **1995**, *142*, L121.
(27) He, R. H.; Li, Q. F.; Xiao, G.; Bjerrum, N. J. *J. Membr. Sci.* **2003**, *226*, 169.
(28) Xiao, L.; Zhang, H.; Jana, T.; Scanlon, E.; Chen, R.; Choe, E. W.; Ramanathan, L. S.; Yu, S.; Benicewicz, B. C. *Fuel Cells* **2005**, *5*, 287.
(29) Xiao, L. X.; Zhang, H. F.; Scanlon, E.; Ramanathan, L. S.; Choe, E. W.; Rogers, D.; Apple, T.; Benicewicz, B. C. *Chem. Mater.* **2005**, *17*, 5328.
(30) Dai, H.; Zhang, H.; Zhong, H.; Jin, H.; Li, X.; Xiao, S.; Mai, Z. *Fuel Cells* **2010**, *10*, 754.
(31) Kumbharkar, S. C.; Islam, M. N.; Potrekar, R. A.; Kharul, U. K. *Polymer* **2009**, *50*, 1403.
(32) Yamaguchi, T.; Nakao, S.; Kimura, S. *Macromolecules* **1991**, *24*, 5522.
(33) Yameen, B.; Kaltbeitzel, A.; Glasser, G.; Langner, A.; Muller, F.; Gosele, U.; Knoll, W.; Azzaroni, O. *ACS Appl. Mater. Interfaces* **2010**, *2*, 279.
(34) Yamauchi, A.; Ito, T.; Yamaguchi, T. *J. Power Sources* **2007**, *174*, 170.
(35) Li, H. B.; Nogami, M. *Adv. Mater.* **2002**, *14*, 912.
(36) Bureekaew, S.; Horike, S.; Higuchi, M.; Mizuno, M.; Kawamura, T.; Tanaka, D.; Yanai, N.; Kitagawa, S. *Nat. Mater.* **2009**, *8*, 831.
(37) Hogarth, W. H. J.; da Costa, J. C. D.; Drennan, J.; Lu, G. Q. *J. Mater. Chem.* **2005**, *15*, 754.
(38) Huang, Y.; Li, Q. F.; Jensen, A. H.; Yin, M.; Jensen, J. O.; Christensen, E.; Pan, C.; Bjerrum, N. J.; Xing, W. *J. Mater. Chem.* **2012**, *22*, 22452.
(39) Huang, Y. J.; Li, Q. F.; Anfimova, T. V.; Christensen, E.; Yin, M.; Jensen, J. O.; Bjerrum, N. J.; Xing, W. *Int. J. Hydrogen Energy* **2013**, *38*, 2464.
(40) Paschos, O.; Kunze, J.; Stimming, U.; Maglia, F. *J. Phys.: Condens. Matter* **2011**, *23*, 234110.
(41) Nogami, M.; Daiko, Y.; Goto, Y.; Usui, Y.; Kasuga, T. *J. Sol-Gel Sci. Technol.* **2003**, *26*, 1041.
(42) Mosa, J.; Larramona, G.; Duran, A.; Aparicio, M. *J. Membr. Sci.* **2008**, *307*, 21.
(43) Munakata, H.; Ochiai, S.; Kanamura, K. *J. Electrochem. Soc.* **2007**, *154*, B871.
(44) Zeng, J.; Zhou, Y. H.; Li, L.; Jiang, S. P. *Phys. Chem. Chem. Phys.* **2011**, *13*, 10249.
(45) Halla, J. D.; Mamak, M.; Williams, D. E.; Ozin, G. A. *Adv. Funct. Mater.* **2003**, *13*, 133.
(46) Marschall, R.; Bannat, I.; Feldhoff, A.; Wang, L. Z.; Lu, G. Q.; Wark, M. *Small* **2009**, *5*, 854.
(47) Jiang, B. Y.; Tang, H. L.; Pan, M. *Int. J. Hydrogen Energy* **2012**, *37*, 4612.
(48) Mishra, A. K.; Kuila, T.; Kim, D. Y.; Kim, N. H.; Lee, J. H. *J. Mater. Chem.* **2012**, *22*, 24366.
(49) Sel, O.; Azais, T.; Marechal, M.; Gebel, G.; Laberty-Robert, C.; Sanchez, C. *Chem.—Asian J.* **2011**, *6*, 2992.
(50) Jin, Y. G.; Qiao, S. Z.; Xu, Z. P.; Yan, Z. M.; Huang, Y. N.; da Costa, J. C. D.; Lu, G. Q. *J. Mater. Chem.* **2009**, *19*, 2363.
(51) Marschall, R.; Tolle, P.; Cavalcanti, W. L.; Wilhelm, M.; Kohler, C.; Frauenheim, T.; Wark, M. *J. Phys. Chem. C* **2009**, *113*, 19218.
(52) Lu, S. F.; Wang, D. L.; Jiang, S. P.; Xiang, Y.; Lu, J. L.; Zeng, J. *Adv. Mater.* **2010**, *22*, 971.
(53) Tang, H. L.; Pan, M.; Jiang, S. P. *Dalton Trans.* **2011**, *40*, 5220.
(54) Zeng, J.; He, B.; Lamb, K.; De Marco, R.; Shen, P. K.; Jiang, S. P. *Chem. Commun.* **2013**, *49*, 4655.
(55) Kleitz, F.; Liu, D. N.; Anilkumar, G. M.; Park, I. S.; Solovyov, L. A.; Shmakov, A. N.; Ryoo, R. *J. Phys. Chem. B* **2003**, *107*, 14296.
(56) Kleitz, F.; Choi, S. H.; Ryoo, R. *Chem. Commun.* **2003**, 2136.
(57) Kleitz, F.; Solovyov, L. A.; Anilkumar, G. M.; Choi, S. H.; Ryoo, R. *Chem. Commun.* **2004**, 1536.
(58) Ravikovitch, P. I.; Neimark, A. V. *Langmuir* **2002**, *18*, 9830.
(59) Morishige, K.; Tateishi, N. *J. Chem. Phys.* **2003**, *119*, 2301.
(60) Zeng, J.; Shen, P. K.; Lu, S.; Xiang, Y.; Li, L.; De Marco, R.; Jiang, S. P. *J. Membr. Sci.* **2012**, *397-398*, 92.
(61) Wan, Y.; Zhao, D. Y. *Chem. Rev.* **2007**, *107*, 2821.
(62) Liang, W. J.; Hsieh, S. J.; Hsu, C. Y.; Chen, W. F.; Kuo, P. L. *J. Polym. Sci., Part B: Polym. Phys.* **2006**, *44*, 2135.
(63) Donia, A. M.; Atia, A. A.; Daher, A. M.; Elshehy, E. A. *J. Dispersion Sci. Technol.* **2011**, *32*, 193.
(64) Boonchom, B.; Danvirutai, C.; Youngme, S.; Maensiri, S. *Ind. Eng. Chem. Res.* **2008**, *47*, 7642.
(65) Weber, J.; Kreuer, K.-D.; Maier, J.; Thomas, A. *Adv. Mater.* **2008**, *20*, 2595.
(66) Nagao, M.; Takeuchi, A.; Heo, P.; Hibino, T.; Sano, M.; Tomitab, A. *Electrochem. Solid State Lett.* **2006**, *9*, A105.
(67) Boysen, D. A.; Uda, T.; Chisholm, C. R. I.; Haile, S. M. *Science* **2004**, *303*, 68.
(68) Uma, T.; Nogami, M. *J. Membr. Sci.* **2009**, *334*, 123.
(69) Zhang, J.; Tang, Y.; Song, C.; Xia, Z.; Li, H.; Wang, H.; Zhang, J. *Electrochim. Acta* **2008**, *53*, 5315.
(70) Mamlouk, M.; Scott, K. *Int. J. Energy Res.* **2010**, *35*, 507.